



UNIVERSIDADE ESTADUAL DE CAMPINAS
SISTEMA DE BIBLIOTECAS DA UNICAMP
REPOSITÓRIO DA PRODUÇÃO CIENTÍFICA E INTELLECTUAL DA UNICAMP

Versão do arquivo anexado / Version of attached file:

Versão do Editor / Published Version

Mais informações no site da editora / Further information on publisher's website:

https://www.scielo.br/scielo.php?script=sci_arttext&pid=S0104-66322019000200797

DOI: 10.1590/0104-6632.20190362s20180280

Direitos autorais / Publisher's copyright statement:

©2019 by Springer. All rights reserved.

DIRETORIA DE TRATAMENTO DA INFORMAÇÃO

Cidade Universitária Zeferino Vaz Barão Geraldo

CEP 13083-970 – Campinas SP

Fone: (19) 3521-6493

<http://www.repositorio.unicamp.br>

CHARACTERIZATION-PERFORMANCE OF ZnO AND ZnO/ZnFe₂O₄ CATALYST USING ARTIFICIAL AND SOLAR LIGHT FOR MERCURY (II) REDUCTION

Ana L. S. Coelho¹, Ambrósio F. de Almeida Neto², Flávio F. Ivashita³,
Giane G. Lenzi^{4*}, Luiz M. de M. Jorge¹ and Onélia A. A. dos Santos¹

¹ Universidade Estadual de Maringá, Departamento de Engenharia Química, Maringá, Paraná, Brazil. ORCID: 0000-0001-6370-0782;
ORCID: 0000-0003-1869-1957; ORCID: 0000-0002-1551-9134

² Universidade Estadual de Campinas, Faculdade de Engenharia Química, Campinas, São Paulo, Brazil. ORCID: 0000-0001-7815-0277

³ Universidade Estadual de Maringá, Departamento de Física, Maringá, Paraná, Brazil. ORCID: 0000-0003-2006-1700

⁴ Universidade Tecnológica Federal do Paraná, Departamento de Engenharia Química, Ponta Grossa, Paraná, Brazil.
E-mail: gianeg@utfpr.edu.br - ORCID: 0000-0003-2065-9622

(Submitted: June 23, 2018 ; Revised: November 8, 2018 ; Accepted: January 7, 2019)

Abstract - This study describes the application of ZnO commercial oxide and ZnO/ZnFe₂O₄ mixed oxides to reduce the mercury ion (Hg²⁺) in the aqueous phase. The catalysts synthesized were characterized by thermogravimetric analysis, adsorption and desorption of N₂, scanning electron microscopy, X-ray diffraction, Fourier transform infrared spectroscopy, photoacoustic spectroscopy and Mössbauer spectroscopy. The heterogeneous photocatalysis process was studied in synthetic effluent treatment containing mercury chloride (HgCl₂) in a batch and solar reactor. The results indicated that commercial ZnO catalyst totally reduced the Hg (II), in all conditions and reaction systems studied. On the other hand, for the mixed oxides (ZnO/ZnFe₂O₄), there was a decrease in the reduction efficiency in the batch reactor, indicating no ability to reduce Hg(II) in the presence of sunlight.

Keywords: Mercury Reduction; Zinc ferrite; Zinc oxide; Heterogeneous photocatalysis.

INTRODUCTION

Nowadays, one of the main environmental problems is the increasing contamination of water bodies by an excess of heavy metals, such as mercury (Hg), which is not only an environmental hazard, but also a serious public health problem (Zhou et al., 2017; Mudasir et al., 2016; Botta et al.2002).

Once present in water bodies, Hg is mainly in the form of HgCl₂. Particles containing Hg²⁺ can also be methylated by the action of specific bacteria, such as *Desulfovibrio desulfuricans* ND132 and *Geobacter sulfurreducens* PCA, resulting in monomethylmercury (MMHg, CH₃Hg⁺) and dimethylmercury (DMHg,

CH₃HgCH₃), which are considered the most toxic forms of Hg (Pieve et al., 2014).

In this context, heterogeneous photocatalysis is a promising environmental decontamination method, since it allows not only the removal of recalcitrant substances, but also their complete mineralization, avoiding the deposition of these compounds in the receiving aquatic bodies (Lenzi et al., 2011).

Several photocatalytic studies employ the use of titanium dioxide (TiO₂) as a semiconductor. However, zinc oxide (ZnO) has a considerably higher electron mobility (200-300 cm²V⁻¹s⁻¹) than TiO₂ (0.1-4 cm²V⁻¹s⁻¹), which favors a greater efficiency in the transfer of the electrons. In addition, the ZnO valence band is

* Corresponding author: Giane G. Lenzi - E-mail: gianeg@utfpr.edu.br

positioned slightly below the corresponding TiO_2 band, so the hydroxyl radicals generated by ZnO (+3.06 V) have a higher oxidation potential when compared to those generated by TiO_2 (+2.7 V) (Kumar et al., 2015; Mohamed et al., 2014). Therefore, ZnO absorbs more of the solar spectrum than other semiconductors, and it is considered an ideal material to be used in the presence of solar energy (Kumar et al., 2015; Mohamed et al., 2014; Lee et al., 2016).

Zinc ferrite (ZnFe_2O_4) presents great potential for application in heterogeneous photocatalysis processes since it is low cost and has a stable structure. Besides, it presents a band gap of 1.9 eV, which makes it a promising material for photocatalytic applications under sunlight.

The recombination of the generated charges (e^-/h^+) constitutes the major limitation of the heterogeneous photocatalysis process, because when the recombination occurs, the electron returns to its valence band without reacting with the species adsorbed on the surface of the semiconductor, dissipating the energy in the form of heat (Pelaez et al., 2012; Rengaraj et al., 2007). Several strategies have been adopted with the purpose of increasing the photocatalytic efficiency. These can be changes in the semiconductor structure and morphology, such as the synthesis of heteroconjugate structures and the distribution of the charges on the surfaces of the photocatalyst, or chemical modifications in the reaction medium, by adding an agent of sacrifice, for example, oxygen, methanol, ethanol, formic acid, oxalic acid, humic acid and others (Wang et al., 2013; Jang et al., 2012; López-Muñoz et al., 2011).

Mercuric species in solution cannot be bio- or chemically degraded (Bota et al., 2002). However, the possibility of the sorbent being reduced or not is very dependent on its standard reduction potential after the adsorption process (Rahman, et al., 2016). pH determines the specification of metal ions and therefore affects the ability of Hg (II) to be adsorbed (Rahman, et al., 2016) onto the ZnO/ ZnFe_2O_4 materials.

The microstructural properties of the photocatalyst particles are specific and related to the synthesis method, for this reason different techniques are used, such as precipitation, microemulsion, thermal decomposition (Music et al., 2002), ion exchange, chemical vapor deposition (Wang et al., 2013), sol-gel (Lenzi et al., 2011), among others. However, a considerable part of such methodologies is associated with high production costs, which make its application inappropriate for developing countries (Mudasir et al., 2016). In this context, impregnation with excess solvent is a promising technique since it is simple and inexpensive (Hameed et al., 2014).

The objective of this work was to study commercial ZnO and ZnO/ ZnFe_2O_4 mixed oxides in the

photocatalytic reduction of Hg^{2+} present in synthetic effluent containing mercury chloride (HgCl_2) in solar and batch reactive systems.

EXPERIMENTAL

Preparation of catalysts

The commercial oxides and the precursor metal salt employed to prepare the catalysts were: zinc oxide (Dynamic, 99.9% purity) and iron (III) nitrate nonahydrate (Sigma-Aldrich, 99.9% purity). The reagents used for the standard reaction solutions were: mercuric chloride - HgCl_2 (Merck P.A); formic acid (Synth, 85% P.A) and nitric acid (Synth, 65% P.A).

Characterization of catalysts

Thermogravimetric Analysis (TGA) and Differential Scanning Calorimetry (DSC)

The TGA and DSC analyses were performed with a Shimadzu TGA-50M Thermogravimetric Analyzer equipment and Mettler Toledo Analytical Microbalance model MX5. A solid mass of 1g was used in the analyses. The temperature range used for the TGA analyses was between room temperature and 1273 K. For the DSC analysis the temperature range was between room temperature and 773 K. The volumetric flow rate of the treatment gas, nitrogen (N_2), was maintained at $50 \text{ mL}\cdot\text{min}^{-1}$, with a heating rate of $10 \text{ K}\cdot\text{min}^{-1}$ used in all experiments.

X-ray diffraction (XRD)

The diffractograms for calcined and non-calcined samples, prepared by the excess solvent impregnation method, as well as pure commercial oxide (ZnO) were obtained on a Bruker D8 Advance X-ray diffractometer using $\text{CuK}\alpha$ radiation ($V = 40 \text{ KV}$, $I = 35 \text{ mA}$). Data were analyzed according to JCPDS (Joint Committee on Powder Diffraction Standards) and ICDD (International Center for Diffraction Data).

Nitrogen Adsorption-Desorption Measurements (N_2)

The specific surface area (S_g), pore volume (V_p) and average pore radius (R_p) as well as the adsorption isotherms, were determined on a Quanta Chrome model Nova 1200 using adsorption of N_2 at 77 K. The non-calcined and calcined samples had been previously submitted to a thermal treatment at 373 K and 573 K, for 8 hour under vacuum to eliminate any existing water within the pores of the solids.

Scanning Electron Microscopy (SEM)

For the micrographs a scanning electron microscope with a dispersive energy X-ray detector, Leo Electron Microscopy, model MEV Leo 440i, was used. For the X-ray spectra the acceleration voltage was 20 kV and the beam current at 700 pA. For coating the samples,

a Sputter Coater Emitech metallic coating equipment, model K450, was used and the thickness of the gold layer was estimated at 200 Å.

Mössbauer spectroscopy

The analyses with Mössbauer Spectroscopy were performed at room temperature in a spectrometer (Halder Elektronik GmbH model MA 531). The equipment was calibrated with a metallic iron absorber, and measurements using ⁵⁷Fe as a nuclear probe were performed by means of ⁵⁷Fe γ radiation emitted by a ⁵⁷Co(Rh) source. For the Mössbauer spectroscopy measurements, the powder samples were encapsulated in small cylindrical containers (sample holder) of acrylic, with approximately 25 mg·cm⁻², an amount calculated to optimize this measurement.

Photoacoustic Spectroscopy

Photoacoustic spectroscopy was used to determine the minimum excitation energy of the conduction band electrons for the valence band, which correspond to the band gap energy. The analysis conditions were: 0.2 g of sample, frequency of 23Hz, sampling timing of 300 ms with 3 means and waiting time of 1s per measurement, slot of 3.16, BP/F/2F filter and gain of 12.

Fourier Transform Infrared Spectroscopy (FTIR)

Measurements of infrared transmittance (FTIR) were performed using Bruker Spectrometer, with a resolution of 4 cm⁻¹; 128 scans; spectral range 400-4000 cm⁻¹.

Reaction Systems

Calcined pure commercial oxide and catalysts, prepared by the impregnation method with excess solvent and calcined, were evaluated in the photocatalytic reduction of Hg(II). The reduction tests were carried out in the liquid phase in a bench scale photocatalytic reaction unit (using ultraviolet irradiation supplied by a 250 W mercury vapor lamp) and in a solar reactor. The reaction time was 3 hours to quantify the decrease in the concentration of Hg(II). During this reaction, samples were collected at regular intervals (0, 2, 5, 10, 15, 30, 60, 90, 120 and 180 minutes) and were filtered (0.45 μm Millipore membrane) for catalyst removal. The remaining concentration of Hg(II) in solution was determined by atomic absorption spectrophotometry (SpectAA - 10 Plus VARIAN). 1 g·L⁻¹ of catalyst was used for the photocatalytic tests.

To efficiently evaluate the Hg(II) reduction, four different reaction conditions were used: solution of Hg²⁺ (120 mg·L⁻¹) (C1); solution of Hg²⁺ (120 mg·L⁻¹) in the presence of formic acid (10mM) as a hole scavenger (C2); solution of Hg²⁺ (120 mg·L⁻¹) in the

presence of oxygen as an electron scavenger (C3); solution of Hg²⁺ (120 mg·L⁻¹) in the presence of oxygen and formic acid.) (C4).

RESULTS AND DISCUSSION

Characterization of catalysts

The TGA / DSC profiles obtained for the mixed oxides containing 5 and 15% wt. Fe are shown Figure 1.

The TGA profiles indicated that the percentage mass loss is more evident for the sample containing the initial nominal metallic load of 15% wt. Fe, possibly due to the higher percentage of iron nitrate in the sample, thus resulting in a greater decomposition of the precursor. The mass loss observed from room temperature up to 400 °C is attributed to the H₂O adsorbed on the catalyst surface. After 400 °C, the mass of the sample remains practically constant, indicating thermal stability from this temperature on. The results of DSC were also equivalent, and they detected endothermic and exothermic peaks, which justify the effects of the heat associated with chemical reactions and physical alterations, in which the endothermic peaks related to the loss of mass were associated with dehydration and decomposition, while the exothermic peaks explain the possible physical changes of the crystallization and oxidation reactions (Kanade et al., 2006).

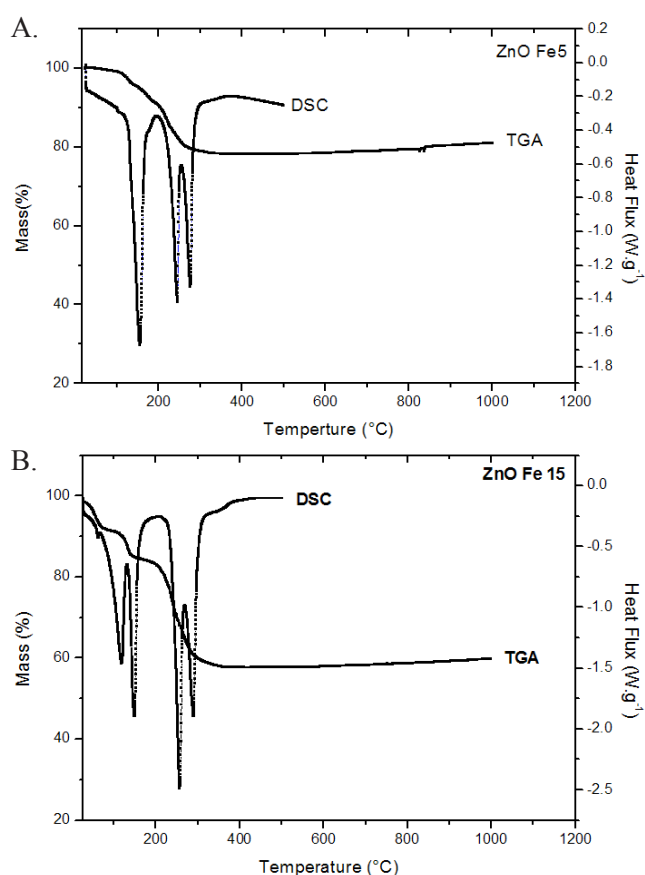


Figure 1. Profile of the TGA/DTGA analysis for the ZnO/ZnFe₂O₄ samples.

The diffractograms obtained for the commercial ZnO, as well as for the non-calcined ZnO/ZnFe₂O₄ 5 (nc) and ZnO/ZnFe₂O₄ 15 (nc) samples, are shown in Fig 2A. The results for the same samples after the thermal treatment can be observed in Fig 2B.

The thermal treatment did not change the crystallinity profile of the commercial sample, the presence of peaks ($2\theta = 31.78^\circ, 34.44^\circ, 36.27^\circ, 47.55^\circ, 56.60^\circ, 67.84^\circ, 66.97^\circ, 67.94^\circ$ and 69.08°) relative to ZnO being wurtzite according to JCPDS PDF # 36-1451 (Chakma et al., 2013; Nirmala et al., 2010).

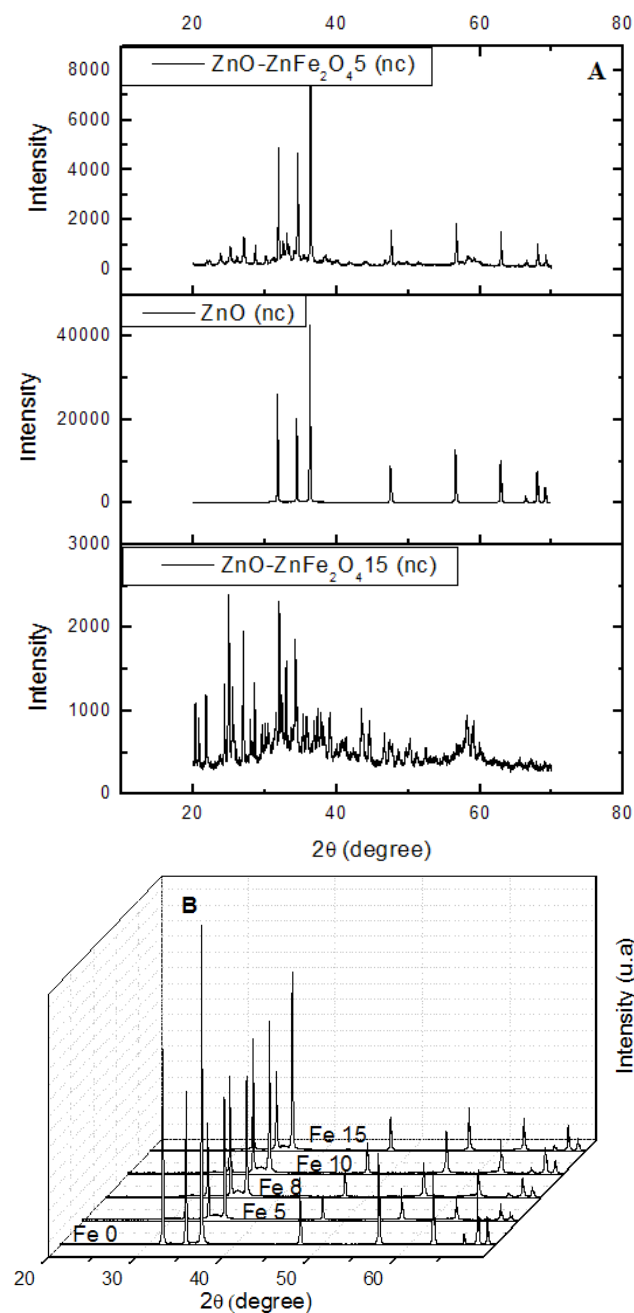


Figure 2. XRD spectra for (2A) noncalcined and (2B) calcined samples, ZnO (Fe 0); ZnO/ZnFe₂O₄ 5 (Fe 5); ZnO/ZnFe₂O₄ 8 (Fe 8); ZnO/ZnFe₂O₄ 10 (Fe 10); ZnO/ZnFe₂O₄ 15 (Fe 15).

The diffractograms obtained for samples containing noncalcined iron present a typical profile of amorphous material, which demonstrates the need for thermal treatment to arrange the atoms in the crystal and obtain a crystalline phase. The samples with 5 and 15wt% Fe in the ZnO matrix, submitted to the calcination process, presented the same crystallinity profile obtained for the pure ZnO. However, zinc ferrite peaks (ZnFe₂O₄) were observed in the samples according to ICSD 22-1012 (Tadjarodi et al., 2015; Carvalho et al., 2017).

Similar results were obtained for the nominal catalysts metal loads of 8 and 10 wt% Fe. In fact, according to Qamar et al. (2017), the wet impregnation technique favors the interaction of Fe³⁺ ions with the oxygen present on the ZnO surface, originating zinc ferrite.

Therefore, in Table 1, it is possible to analyze data of the interplanar space (d-spacing) and width at half height (FWHM). For the FWHM parameter, the results show that the variation obtained between the ZnO/ZnFe₂O₄ and commercial oxide samples was approximately 0.01, while for the d-spacing parameter, a constancy of 2.47 was obtained. Thus, the difference obtained is too small to indicate any significant change in the ZnO crystalline structure due to the presence of zinc ferrite. According to Gonçalves et al. (2017), the differences observed may be due to defects in the structure of the semiconductor caused during the synthesis process, and these are responsible for small changes in the network parameters of the material under analysis. In addition, something similar is observed in the peak heights, indicating that the crystallite size samples are equivalent (Liu et al., 2014).

Fig 3 shows the micrographs for the ZnO/ZnFe₂O₄ 15 sample, again observing the effect of calcination on the structure of the catalysts, which led to the restructured oxides with the formation of ZnFe₂O₄, as observed in the X-ray diffractograms.

The results of Fourier Transform Infrared Spectroscopy (FT-IR) obtained for pure commercial oxide and the calcined ZnO/ZnFe₂O₄ samples, as well as the ZnO/ZnFe₂O₄ 8 (nc) photocatalyst are shown in Fig. 4.

The bands present in the range of 400-700 cm⁻¹ are attributed to Zn-O vibrations (Chakma et al., 2013; Khan et al., 2010; Becheri et al., 2008) while peaks around 1378 cm⁻¹ denote H-O-H vibrations present in

Table 1 DRX data for the calcined ZnO and ZnO/ZnFe₂O₄ samples.

| Samples | 2θ | d-spacing (Å) | FWHM |
|---|----------|---------------|---------|
| ZnO | 36.2700° | 2.47480 | 0.0648° |
| ZnO/ZnFe ₂ O ₄ 5 | 36.3100° | 2.47189 | 0.0756° |
| ZnO/ZnFe ₂ O ₄ 8 | 36.2488° | 2.47620 | 0.0756° |
| ZnO/ZnFe ₂ O ₄ 10 | 36.3613° | 2.47487 | 0.0540° |
| ZnO/ZnFe ₂ O ₄ 15 | 36.2904° | 2.47346 | 0.0648° |

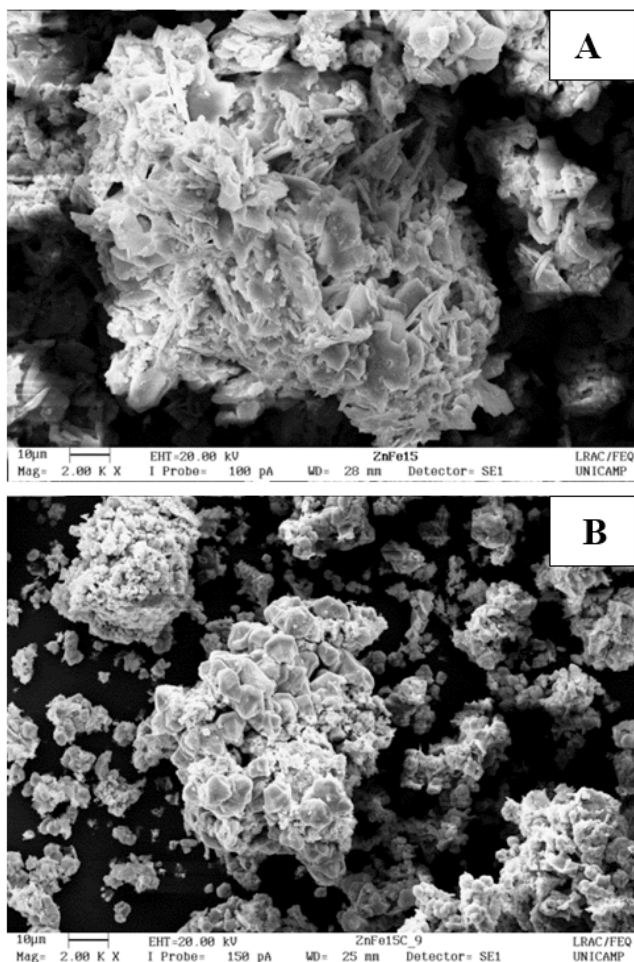


Figure 3. Scanning Electron Micrographs of the ZnO/ZnFe₂O₄ 15 catalyst (A) noncalcined and (B) calcined, increase: 20000x.

the ZnO crystals structure, which may be derived from the water used during the semiconductor synthesis (Raja et al., 2014). The vibrations between 3450 and 3500 cm⁻¹ indicate the presence of hydroxyl OH groups (Maya-Treviño et al., 2015; Chakma et al., 2013; Khan and Khalid, 2010). According to Chakma et al., 2013 and Pandiyarajan et al., 2012, the peaks that appear between 800 and 500 cm⁻¹ can be attributed to Fe³⁺ on the ZnFe₂O₄ surface (Qamar et al., 2017). It is also observed that, with the iron percentage increase, the peaks corresponding to the H-O-H and Zn-O groups are minimized, while the band in the range 800-1500 cm⁻¹ becomes more intense. Such behavior may be related to the fact that O-H clusters act as nucleation sites on which fine ferrite crystals can grow (Ameer et al., 2015). In the non-calcined sample different profiles of molecular vibration was observed comparing with the calcined samples.

In Figure 4B, the bands from 3700 to 3300 cm⁻¹ are related to the symmetric and asymmetric stretches of the hydroxyl groups of H₂O molecules and those located between 669 and 836 cm⁻¹ correspond to the iron atoms

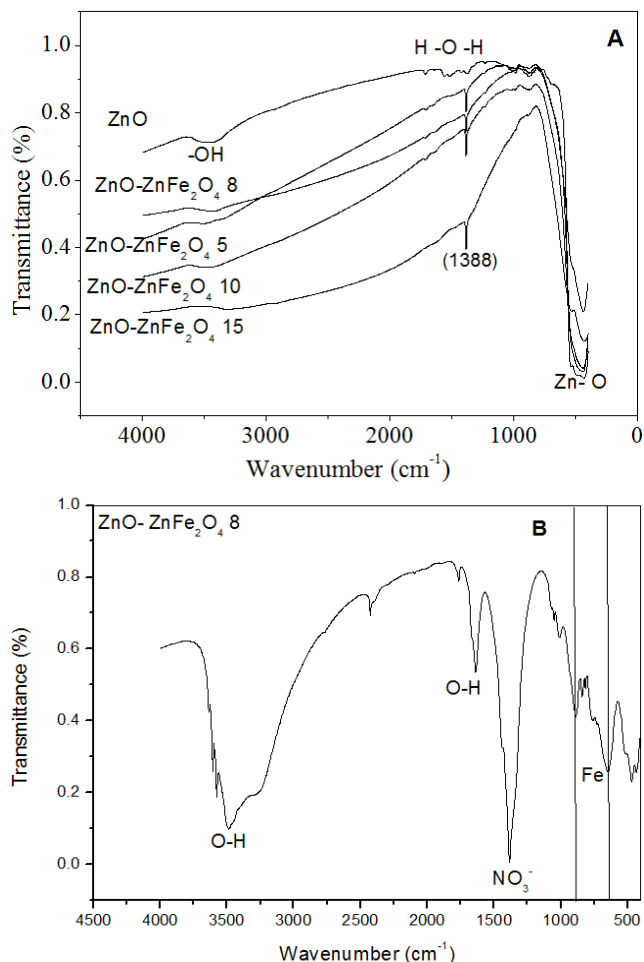


Figure 4. FTIR spectra of samples ZnO e ZnO/ZnFe₂O₄ calcined and ZnO/ZnFe₂O₄ 8 noncalcined, (A) ZnO and ZnO/ZnFe₂O₄ samples and (B) ZnO/ZnFe₂O₄ 8 (nc).

and at 1380 cm⁻¹, correspond to the stretching caused by NO₃⁻ (Chakma et al., 2013; Khan et al., 2010; Maya-Treviño et al., 2015; Cunha et al., 1996).

The Mössbauer spectra and the hyperfine parameters for the ZnO/ZnFe₂O₄ calcined at 400 °C, are shown in Fig 5 and Table 2, respectively.

The samples had well-defined double-dipoles with isomeric displacements of 0.34 mm.s⁻¹ and quadrupolar displacement 0.47-0.49 mm.s⁻¹. which can be attributed to Fe³⁺ ions dispersed in the octahedral structure. However, zinc oxide exhibits a hexagonal crystalline structure whereas the ZnFe₂O₄ spinel presents two sites in the structure, one tetrahedral and the other octahedral (Tadjarodi et al., 2015; Chinnasamy et al., 2000).

Thus, by means of IS values and spectral area (A = 100%) it is assumed that all the iron present in the sample is contained in ZnFe₂O₄ species (Zhu et al., 2016).

In Fig 6. it is possible to observe the N₂ isotherms obtained for the commercial ZnO and for the oxides

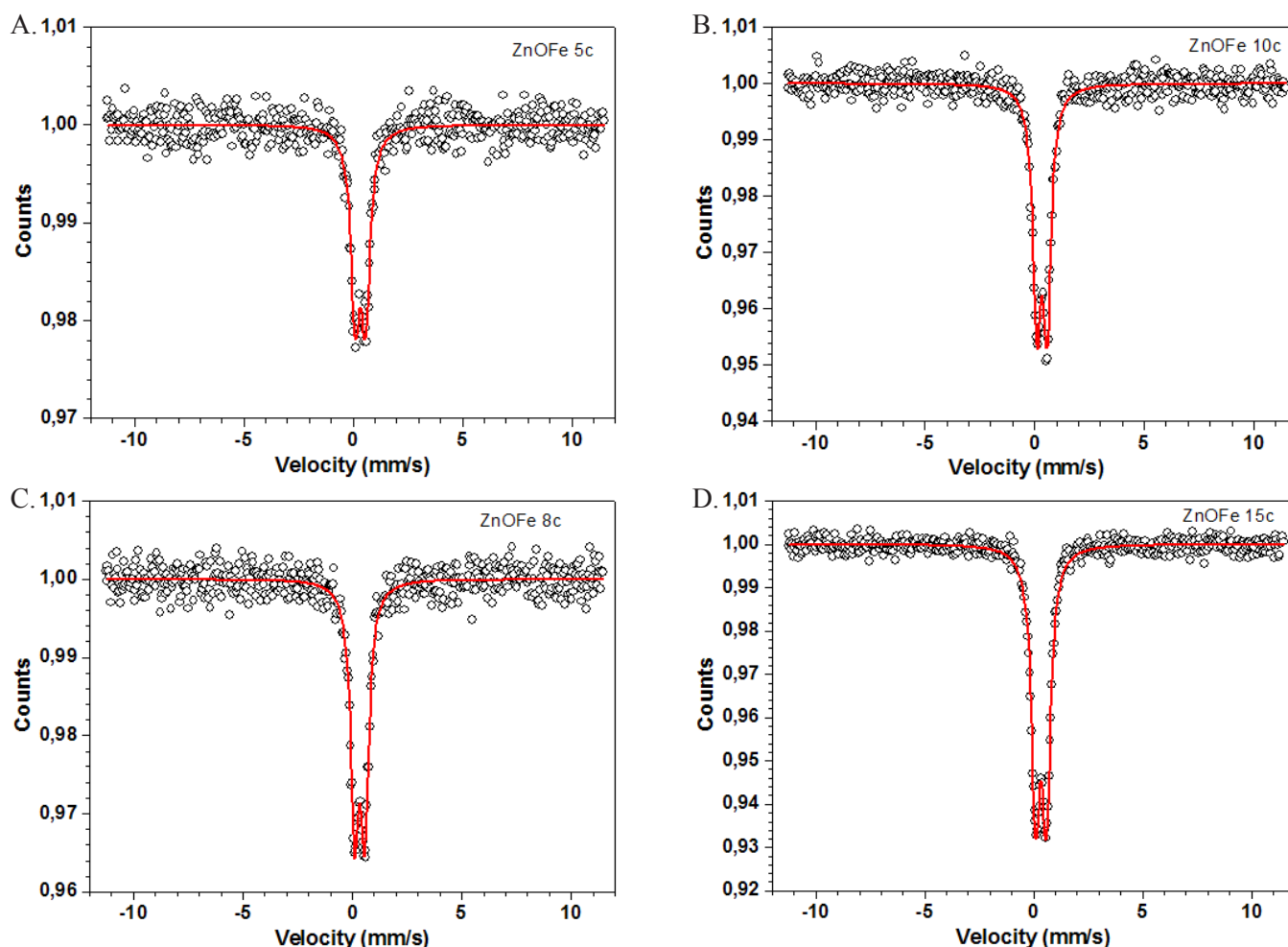


Figure 5. Mössbauer spectra of ZnFe_2O_4 samples.

Table 2 Results of Mössbauer spectra for $\text{ZnO}/\text{ZnFe}_2\text{O}_4$; temperature $\langle T \rangle$, isomer shifts $\langle \text{IS} \rangle$; quadrupole splitting $\langle \text{Qua} \rangle$; absorption area $\langle A \rangle$; magnetic hyperfine field $\langle \text{Bhf} \rangle$.

| Sample | Spectrum | T(K) | $\langle \text{IS} \rangle$ ($\text{mm}\cdot\text{s}^{-1}$) ± 0.01 | $\langle \text{Qua} \rangle$ ($\text{mm}\cdot\text{s}^{-1}$) ± 0.01 | Bhf (T) | A (%) |
|-----------------------------------|----------|------|---|--|------------|----------|
| ZnO/ ZnFe_2O_4 5 | Doublet | 300 | 0.34 | 0.47 | - | 100 |
| ZnO/ ZnFe_2O_4 8 | Doublet | 300 | 0.34 | 0.47 | - | 100 |
| ZnO/ ZnFe_2O_4 10 | Doublet | 300 | 0.34 | 0.47 | - | 100 |
| ZnO/ ZnFe_2O_4 15 | Doublet | 300 | 0.34 | 0.49 | - | 100 |

modified with zinc ferrite. The ZnO and ZnO/ ZnFe_2O_4 10 sample profiles present the type II isotherm, indicating adsorption in superimposed multiple layers predominant in mesoporous structures according to the International Union of Pure and Applied Chemistry (IUPAC).

In the samples ZnO/ ZnFe_2O_4 5, ZnO/ ZnFe_2O_4 8 and ZnO/ ZnFe_2O_4 15, it was verified that the isotherms obtained are similar and predominantly of type V. The semiconductor isotherms also presented hystereses that are associated with mesopore forms. For ZnO/ ZnFe_2O_4 5 and ZnO/ ZnFe_2O_4 samples, a tendency for N_2 hysteresis related to bottle-style mesopores is observed and the ZnO/ ZnFe_2O_4 15 sample shows conical from wedge associated with hysteresis type H3 (IUPAC).

It was observed that the volume of N_2 adsorbed by ZnO and ZnO/ ZnFe_2O_4 15 is higher than those obtained for the other samples, indicating that the interparticle porosity of these materials is higher in comparison to ZnO/ ZnFe_2O_4 5, ZnO/ ZnFe_2O_4 8 and ZnO/ ZnFe_2O_4 10.

Because the volume of N_2 adsorbed by the oxides can be correlated with the values of the specific area of the oxides, the greater the nitrogen adsorption, the greater the specific area of the material (Mandal et al., 2015).

The values obtained from the adsorption-desorption measurements of N_2 for specific surface area (S_g), pore volume (V_p) and average pore radius (R_p), as well as the results obtained from the photoacoustic

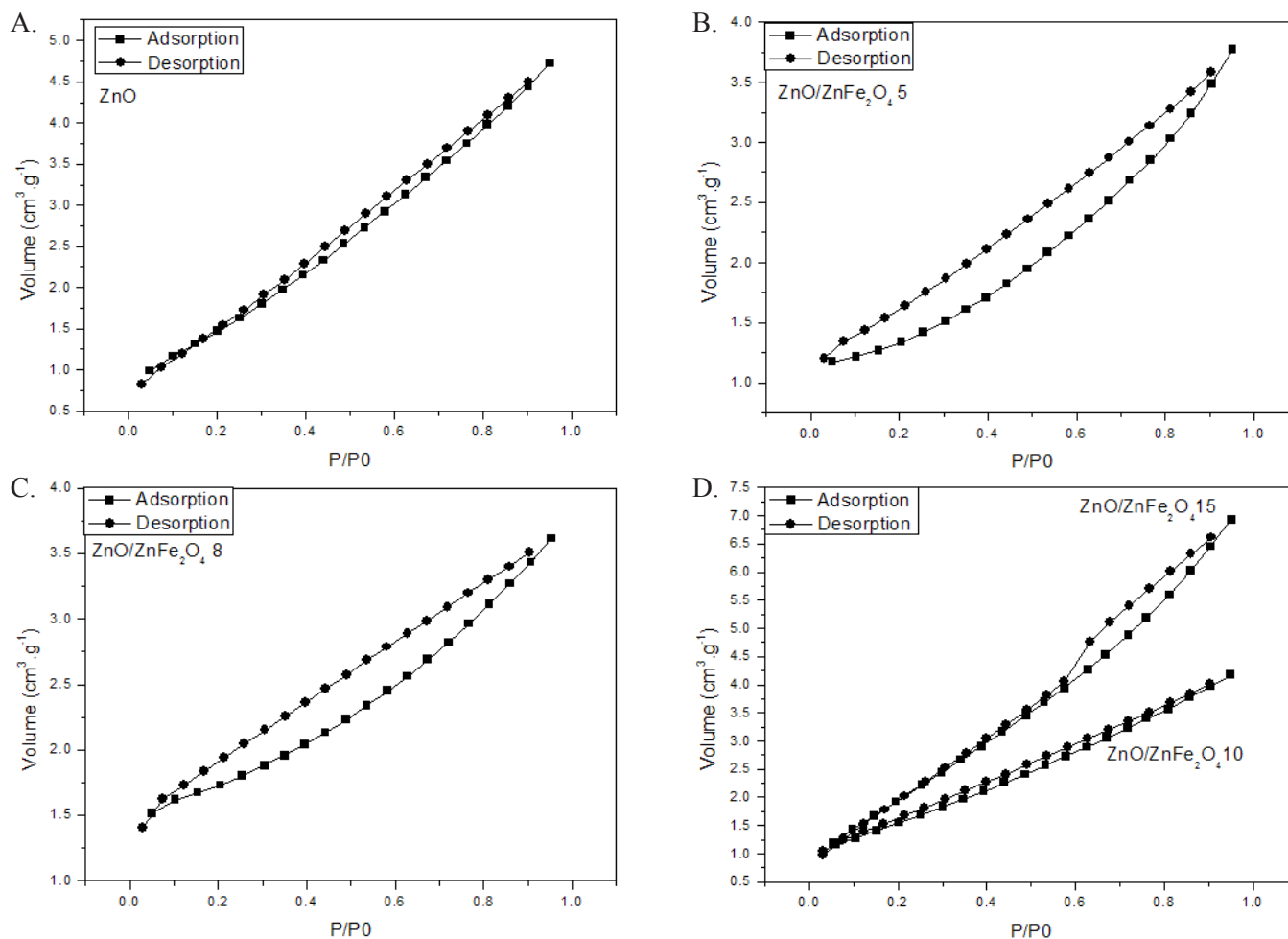


Figure 6. N₂ adsorption-desorption isotherm of commercial ZnO and calcined ZnO/ZnFe₂O₄ samples.

spectroscopy for ZnO and ZnO / ZnFe₂O₄ catalysts are shown in Table 3.

The photoacoustic spectroscopy result for the commercial ZnO was 3.18 eV. In the literature some authors (Mohamed et al., 2014; Ba-Abbad et al., 2013) found a band gap value of 3.37 eV for ZnO, while others (Aydin et al., 2013; Sakthivel et al., 2003) report band gap values for this semiconductor of 3.19 eV and 3.17 eV, respectively. In the ZnO/ZnFe₂O₄ catalyst, a reduction of bandgap energy was generally observed. Based on the Mossbauer spectroscopy and X-ray diffraction results, the formation of heteroconjugated structures between Zn and ZnFe₂O₄ is assumed, which justifies the extension of light absorption to the visible region (Wang et al., 2013).

Table 3. Specific surface area (Sg), pore volume (Vp), average pore radius (Rp) and band gap energy for the ZnO and ZnO/ZnFe₂O₄ catalysts.

| Sample | Sg (m ² .g ⁻¹) | Rp (Å) | Vp (cm ³ .g ⁻¹) | Band gap (eV) |
|---|---------------------------------------|--------|--|---------------|
| ZnO | 5 | 28 | 0.007 | 3.18 |
| ZnO/ZnFe ₂ O ₄ 5 | 4 | 29 | 0.0038 | 1.94 |
| ZnO/ZnFe ₂ O ₄ 8 | 6 | 18 | 0.0032 | 1.83 |
| ZnO/ZnFe ₂ O ₄ 10 | 6 | 23 | 0.0048 | 1.84 |
| ZnO/ZnFe ₂ O ₄ 15 | 8 | 16 | 0.0095 | 1.55 |

Thus, the n-n heterogeneous structure characteristic of ZnO/ZnFe₂O₄ is capable of efficiently separating the photogenerated electrons from the gap, resulting in improved photoactivation under sunlight (Rahimi et al., 2015). This is because the electrons in the valence band (VB) of ZnFe₂O₄ are preferentially excited to their conduction band (CB) under visible light irradiation and therefore generate an equal amount of holes in their VB. The CB level of ZnFe₂O₄ is lower than that of ZnO (0.9 eV). Thus, the photogenerated electrons in the CB of ZnFe₂O₄ can be transferred to that of ZnO. On the other hand, the photogenerated holes are transferred from the VB of the ZnFe₂O₄ to the VB of the ZnO, because the VB level of the ZnO is 2.5 eV higher than the VB of ZnFe₂O₄. Therefore, the probability of electron-hole recombination can be reduced.

Adsorption and photocatalysis tests of Hg(II) reduction

Batch reactor tests were performed in the absence of UV light, before the photocatalytic reduction reactions, to verify the adsorption of mercury(II) on the commercial oxide (ZnO) surface, as well as on

the surface of the calcined synthesized catalysts. The adsorption test results are indicated in Fig. 7.

The pure ZnO, when present in a medium containing an aqueous solution and 120 mg.L⁻¹ of mercuric chloride, did not show the ability to adsorb Hg(II), and the same was observed for an aqueous solution containing mercuric chloride and oxygen (0.83% removal of Hg from the medium). In the presence of the Hg(II) aqueous solution containing formic acid and

oxygen, the adsorptive capacity of the semiconductor in 3 hours was 22% and 19%, respectively.

For the ZnO/ZnFe₂O₄ 5 catalyst, the adsorption percentages of 44.45%, 31.24%, 22% and 19.3% were observed for conditions C1, C2, C3 and C4, respectively. This profile is maintained for the other catalysts. The highest removal percentage was verified for the oxygen-containing solution (33.62%) for calcined ZnO/ZnFe₂O₄ 8 and was also observed for

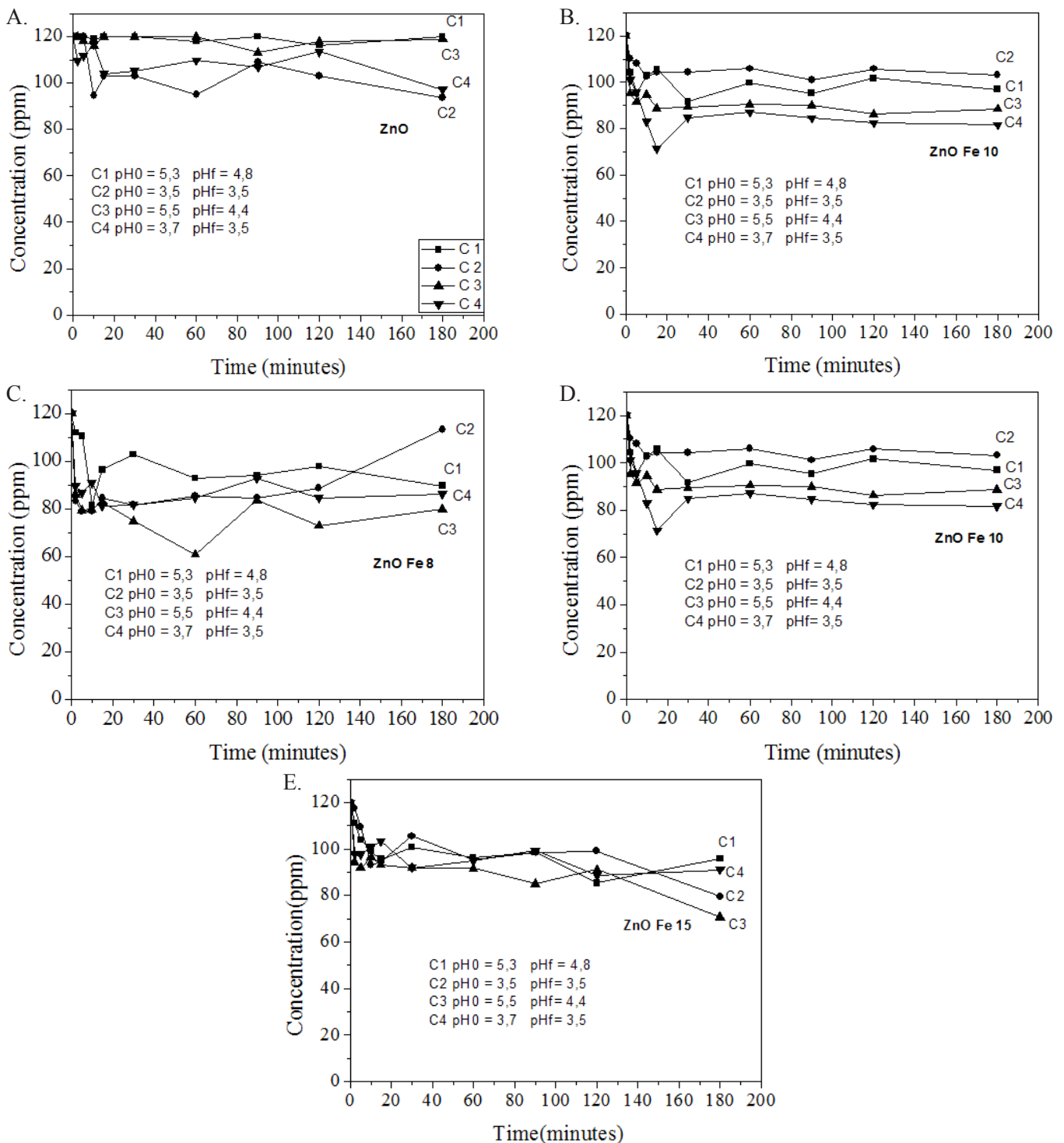


Figure 7. Adsorption of Hg(II) on the ZnO surface and the ZnO/ZnFe₂O₄ catalysts.

calcined ZnO/ZnFe₂O₄ 15 (41%). For calcined ZnO/ZnFe₂O₄ 10, the highest adsorption capacity was obtained for the C4 reaction condition, with a removal of approximately 32%. The pH is one of the factors that most affects the adsorption capacity of metallic ions on the surface of ZnO, because it affects not only the adsorbent structure, but also the adsorbate (Sheela et al., 2012).

In addition, heavy metal adsorption is attributed to different ion exchange mechanisms. The metal ions can move through the catalyst pores, the channels present in the crystalline structure, and may also substitute hydroxyl groups on the semiconductor surface.

In relation to mixed oxides, it was reported that, in aqueous media, the surface of ferritic nanoparticles in the spinel form has a positively or negatively charged surface for acidic or alkaline conditions, respectively (Kefeni. et al., 2017).

This favors anion adsorption at a low pH and cations at basic pH. In addition, there is the speciation of Hg(II) adsorbate in aqueous medium with respect to pH: primarily Hg²⁺ with some HgCl⁺ (pH less than 4.0); predominance of HgCl₂ and traces of Hg(OH)₂ (pH 4-6); HgCl₂, HgOH⁺, Hg₂(OH)₃⁺ and less Hg(OH)₂ (pH 6-8); Hg(OH)₂ (pH greater than 8) (Zhou et al., 2017).

The photocatalytic results using pure ZnO and the ZnO-based catalysts prepared by the excess solvent impregnation method are shown in Fig 8.

According to the results obtained, the catalyst that presented the best performance was pure ZnO, when the reaction was carried out in the reaction medium containing formic acid as hole scavenger. Under these conditions, the mercury photoreduction was fast, with a 100% reduction in the detection limits of the flame atomic absorption spectrometry (FAAS). It was not possible to detect the presence of Hg(II) in the reaction medium after 10 minutes of reaction. In the presence of the aqueous solution containing only mercuric chloride at the concentration of 120 mg.L⁻¹ (C1) and the aqueous solution containing HgCl₂ and oxygen (C3), a complete reduction of the Hg(II) was observed in 30 minutes of reaction, while in the presence of the aqueous solution containing mercuric chloride, oxygen and 10 mM formic acid (C4), the time required for the complete reduction of Hg (II) was 15 minutes.

The photocatalytic activity obtained for ZnO can be attributed to the high number of defects present in its crystalline structure - oxygen, interstitial zinc and interstitial oxygen vacancies - which permits the incorporation of impurities, contaminants or dopants in its reticulum (Kayaci et al., 2014; Ansari et al., 2013). Ong et al. (2018) affirmed that the oxidation/reduction reactions by photocatalysis are dependent on the bandgap energy as well as the OH radicals present on the catalyst surface.

The best performance of the commercial oxide regarding the mixed oxides can be justified based on the results of FTIR. For the ZnO/ZnFe₂O₄ materials, a decrease of the bands corresponding to the H-O-H group compared to ZnO is observed. Such groups may correspond to the adsorption sites of Hg(II), limiting one of the steps of the photocatalytic mechanism.

For the ZnO-based catalysts containing different nominal iron metal charges (ZnO/ZnFe₂O₄), there was a complete removal of Hg(II), although the average time required for this was between 30 and 90 minutes of reaction. The ZnO/ZnFe₂O₄ 5 and ZnO/ZnFe₂O₄ catalysts showed a better performance when the reaction medium was composed of an aqueous solution containing mercury, formic acid and oxygen (C4), in which the time required for complete reduction of Hg(II) was 30 minutes. For the catalysts ZnO/ZnFe₂O₄ 10 and ZnO/ZnFe₂O₄ 15, the reaction medium containing mercuric chloride and formic acid (C2) was the most appropriate one, the time required for the photoreduction of the mercury ion being 30 and 60 minutes, respectively.

Among the synthesized materials, the best performance of the ZnO/ZnFe₂O₄ 5 sample can be justified on the basis of the adsorption and desorption data of N₂. Despite not having the largest specific surface area of the mixed oxides, this sample presents the largest average pore radius. This characteristic may allow better transport from Hg(II) adsorption sites favoring the photocatalytic reduction (Li et al., 2014). According to Cheng et al. (2017), ZnO/ZnFe₂O₄ semiconductor materials that present a high specific area provide a greater amount of active sites for the photocatalytic process, but this characteristic generates a greater amount of defects in the structure of the catalyst, which facilitates the recombination of the electrons and the holes, inhibiting the physical-chemical transformations in the substrate (Liu et al., 2016).

In addition, it is possible that the average pore volume of magnitude 0.0032 cm³.g⁻¹ of the ZnO/ZnFe₂O₄ sample favors better light transmission to the inner cavities of the catalyst (Li et al., 2014). Regarding the presence of sacrificial agents, it is observed that they had a limited contribution in the process of reduction of mercury (Hg²⁺) present in the initial solution. According to studies (Aguado et al., 1995), oxygen exerts the role of inhibitor in the photoreduction process of Hg(II) as it competes with the electrons photogenerated by the semiconductor material. However, formic acid has a counterpart function, reacting with the generated holes, favoring the reduction of mercury (Cai et al., 2016; Wang et al., 2004).

The ZnO and ZnO/ZnFe₂O₄ 5 oxides were used for the catalytic photoreaction experiments under solar radiation. Thus, it was observed that there was very little mercuric ion reduction (Fig 9), which may be linked to

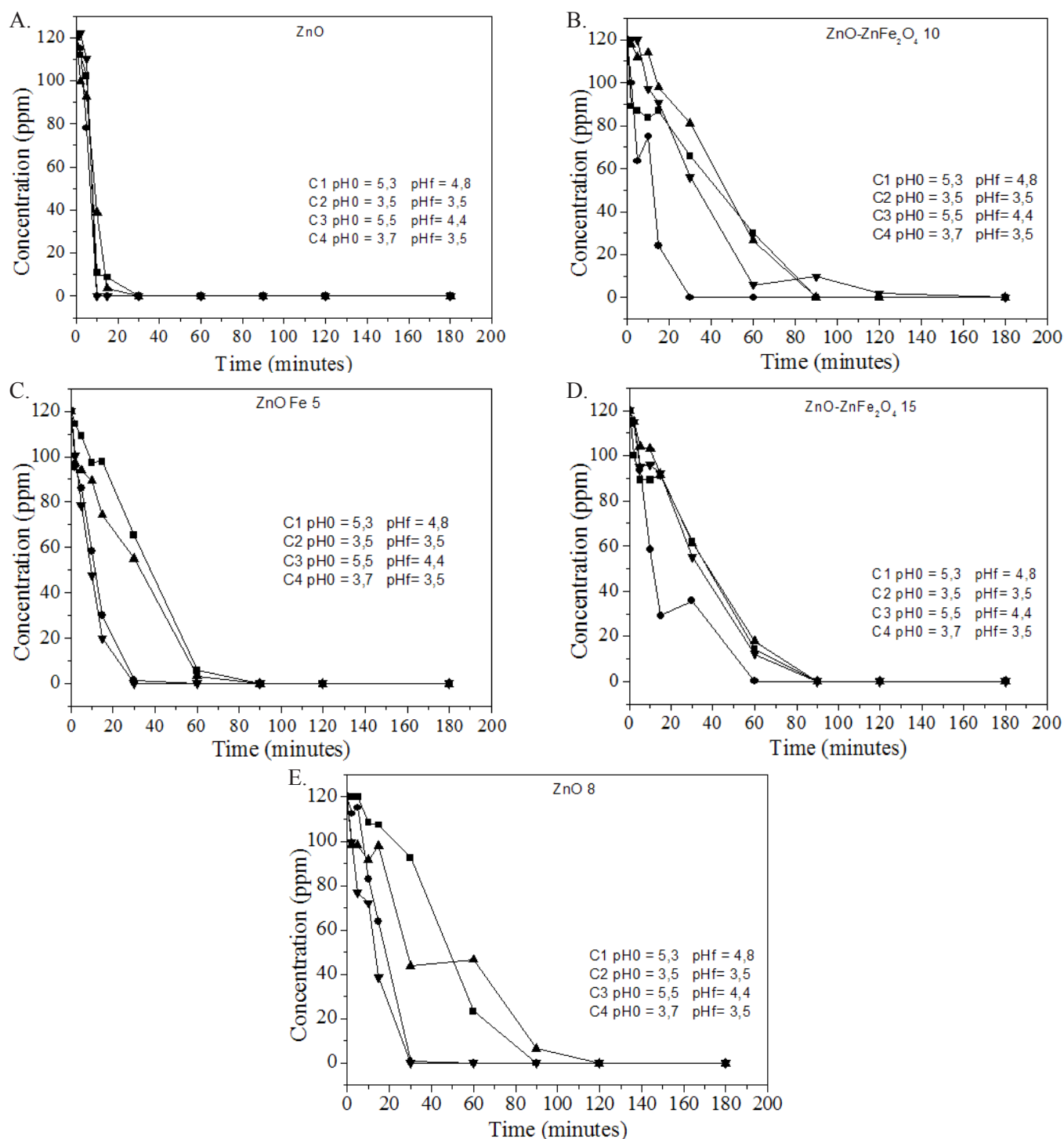


Figure 8. Hg(II) photocatalytic reduction on the ZnO and ZnO/ZnFe₂O₄ catalysts surface.

the bandgap of 1.94 eV - and can be attributed to the presence of ZnO₂Fe₄ - providing a rapid recombination of the electron/hole pairs (e⁻/h⁺) and reducing the quantum efficiency of the material. This problem can be solved by doping the zinc ferrite with Ag, as related in the literature (Harish et al., 2012), or with other materials such as Ca and Gd (Bini et al., 2018).

The photocatalytic performance is significantly influenced by the reaction conditions, such as:

incident light spectrum and intensity, reaction temperature, amount of catalyst, the addition of cocatalysts, the pH of the solution, reactor design and configuration, and so on. Therefore, it is a difficult task to compare the efficiencies of photocatalysts reported under different conditions (Xiao et al., 2018).

In this context, Table 4 indicates reports of different experimental parameters and their results.

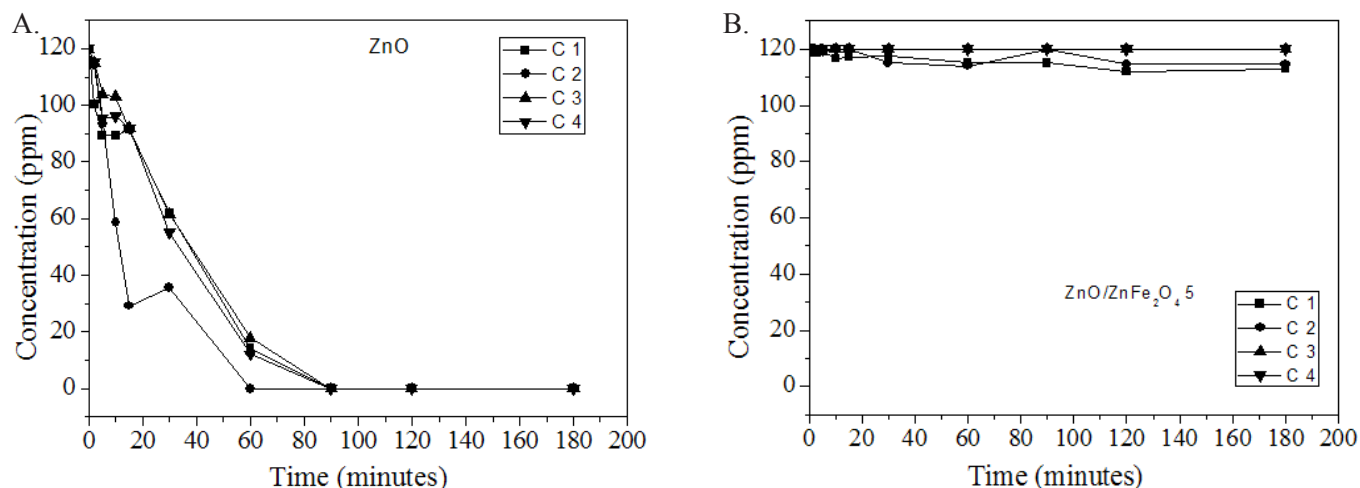


Figure 9. Hg(II) Photocatalytic reduction under solar radiation.

Table 4. Best results of several studies which report Hg(II) photoreduction in an aqueous phase.

| References | Photocatalyst | Reaction time (min) | Removal (%) | Radiation source | Hg final compound | Amount of catalyst (g.L ⁻¹) |
|---------------------------|--|---------------------|-------------|--------------------------------|--|---|
| Aguado et al. (1995) | Titania (Degussa P25) | variable | 100% | UV light | Hg(0) | 0.5 |
| Byrne et al. (2009) | Silica/Titania | 60 | 40 % | UV light | Not reported | 1 |
| López-Muñoz et al. (2011) | TiO ₂ | 180 | 100% | UV irradiation | Hg ₂ Cl ₂ and Hg(0)* Hg(0)** | 0.2-4 |
| Lenzi et al. (2011) | Sol gel TiO ₂ and Ag/TiO ₂ | 180 | 100 % | UV light | Hg (0) | 2 |
| Mohamed et al. (2014) | Carbon nanotubes/Pd-ZnO | 30 | 100% | Visible light | Not reported | 1.2 |
| Mohamed et al. (2015) | SnO ₂ -Co ₃ O ₄ | 30 | 100% | Visible light | Not reported | Not reported |
| Lee et al. (2017) | WO ₃ -TiO ₂ | 120 | 91% | TUV 96 W UV-B Germicidal light | Hg(0) | Not reported |
| Coelho et al. (2017) | TiO ₂ and TiO ₂ /Fe | 180 | 100% | UV light | Hg ₂ Cl ₂ | 1 |
| Coelho et al. (2017) | TiO ₂ and TiO ₂ /Fe | 180 | 67% | Solar radiation | Hg ₂ Cl ₂ | 1 |

*Addition of hole scavenger; ** absence of hole scavenger.

CONCLUSIONS

The pure oxide ZnO presented Hg(II) photoreduction efficiency in the all experimental conditions and reaction systems used in this work. It was also observed that, for reactions carried out in batch reactor in the presence of formic acid, the complete reduction of Hg²⁺ was achieved more quickly. The results indicated that all the ZnO/ZnO₂Fe₄ catalysts were able to reduce Hg(II) under UV light, but a lower efficiency was observed in the photoreduction process of Hg(II) when compared to pure oxide.

ACKNOWLEDGMENTS

The authors wish to thank the Brazilian Agencies CAPES and CNPq for the financial support of this study.

REFERENCES

- Aguado, M. A., Cervera-March, S., Giménez, J. Continuous photocatalytic treatment of mercury (II) on titania powders. Kinetics and catalyst activity. *Chemical Engineering Science*, 50, 1561-1569 (1995). [https://doi.org/10.1016/0009-2509\(95\)00001-L](https://doi.org/10.1016/0009-2509(95)00001-L)
- Ameer, S., Gul, I. H., Mahmood, N., Mujahid, M. Semiconductor-to-metallic flipping in a ZnFe₂O₄-graphene based smart nano-system: Temperature/microwave magneto-dielectric spectroscopy. *Materials Characterization*, 99, 254-265 (2015). <https://doi.org/10.1016/j.matchar.2014.11.018>
- Ansari, S. A., Khan, M., Kalathil, S., Nisar, A., Lee, J., Cho, M. H. Oxygen vacancy induced band gap narrowing of ZnO nanostructures by an electrochemically active biofilm. *Nanoscale*,

- 5, 9238-9246 (2013). <https://doi.org/10.1039/c3nr02678g>
- Aydin, C., Abd El-Saked, M. S., Zheng, K., Yahia, I. S., Yakuphanoglu, F. Synthesis, diffuse reflectance and electrical properties of nanocrystalline Fe-doped ZnO via sol-gel calcination technique. *Optics & Laser Technology*, 48, 447-452 (2013). <https://doi.org/10.1016/j.optlastec.2012.11.004>
- Ba-Abbad, M. M., Kadhum, A. A. H., Mohamad, A. B., Takriff, M. S., Sopian, K. Visible light photocatalytic activity of Fe³⁺-doped ZnO nanoparticle prepared via sol-gel technique. *Chemosphere*, 91, 1604-1611 (2013). <https://doi.org/10.1016/j.chemosphere.2012.12.055>
- Becheri, A., Durr, M., Nostro, P. L. O., Baglioni, P. Synthesis and characterization of zinc oxide nanoparticles: application to textiles as UV-absorbers. *Journal of Nanoparticle Research*, 10, 679-689 (2008). <https://doi.org/10.1007/s11051-007-9318-3>
- Bini, M., Tondo, C., Capsoni, D., Mozzati, M. C., Albini, B., Galinetto, P. Superparamagnetic ZnFe₂O₄ nanoparticles: The effect of Ca and Gd doping. *Materials Chemistry and Physics*, 204, 72-82 (2018). <https://doi.org/10.1016/j.matchemphys.2017.10.033>
- Botta, S. G., Rodriguez, D. J., Leyva, A. G., Litter, M. I. Features of the transformation of Hg^{II} by heterogeneous photocatalysis over TiO₂. *Catalysis Today*, 76, 247-258 (2002). [https://doi.org/10.1016/S0920-5861\(02\)00223-7](https://doi.org/10.1016/S0920-5861(02)00223-7)
- Byrne, H. E., Mazyck, D. W. Removal of trace level aqueous mercury by adsorption and photocatalysis on silica-titania composites. *Journal of Hazardous Materials*, 170, 915-919 (2009). <https://doi.org/10.1016/j.jhazmat.2009.05.055>
- Cai, C., Liu, J., Zhang, Z., Zheng, Y., Zhang, H. Visible light enhanced heterogeneous photo-degradation of Orange II by zinc ferrite (ZnFe₂O₄) catalyst with the assistance of persulfate. *Separation and Purification Technology*, 165, 42-52 (2016). <https://doi.org/10.1016/j.seppur.2016.03.026>
- Carvalho, M. D., Ferreira, L. P., Borges, R. P., Godinho, M. Investigation of the iron site localization in doped ZnO. *Journal of Solid State Chemistry*, 185, 160-165. (2012). <https://doi.org/10.1016/j.jssc.2011.11.006>
- Chakma, S., Bhasarkar, J. B., Moholkar, V. S. Preparation, characterization and application of sonochemically doped Fe³⁺ into ZnO particles. *International Journal of Research in Engineering and Technology*, 2, 177-183 (2013). <https://doi.org/10.15623/ijret.2013.0208030>
- Cheng, M., Liu, D., Deng, Y., Fu, W., Zou, H., Liang, F. Tailoring the porosity of ZnO/ZnFe₂O₄ composites for photocatalytic applications. *Ceramics International*, 43, 16027-16031 (2017). <https://doi.org/10.1016/j.ceramint.2017.08.148>
- Chinnasamy, C. N., Narayanasamy, A., Ponpandian, N., Chattopadhyay, K., Guérault, H., Greneche, J. M. Magnetic properties of nanostructured ferromagnetic zinc ferrite. *Journal of Physics: Condensed Matter*, 12, 7795-7805 (2000). <https://doi.org/10.1088/0953-8984/12/35/314>
- Coelho, A. L. S., Almeida Neto, A. F., Ivashita, F. F., Lenzi, G. G., Jorge, L. M. M., Santos, O. A. A. TiO₂ and modified TiO₂/Fe on photocatalytic reduction of Hg²⁺ using artificial and solar radiation. *Desalination and Water Treatment*, 97, 304-314 (2017). <https://doi.org/10.5004/dwt.2017.21630>
- Cunha, M. C. P., Weber, M., Nart, F. C. On the adsorption and reduction of NO₃⁻ ions at Au and Pt electrodes studied by in situ FTIR spectroscopy. *Journal of Electroanalytical Chemistry*, 414, 163-170 (1996). [https://doi.org/10.1016/0022-0728\(96\)04697-9](https://doi.org/10.1016/0022-0728(96)04697-9)
- Da Pieve, F., Stankowski, M., Hogan, C. Electronic structure calculations of mercury mobilization from mineral phases and photocatalytic removal from water and the atmosphere. *Science of the Total Environment*, 493, 596-605 (2014). <https://doi.org/10.1016/j.scitotenv.2014.06.012>
- Gonçalves, P., Bertholdo, R., Dias, J. A., Maestrelli, S. C., Giraldo, T. R. Evaluation of the photocatalytic potential of TiO₂ and ZnO obtained by different wet chemical methods. *Materials Research-Iberoamerican Journal of Materials*, 20, 181-189 (2017). <https://doi.org/10.1590/1980-5373-mr-2016-0936>
- Hameed, A., Aslam, M., Ismail, I. M., Chandrasekaran, S., Kadi, M. W., Gondal, M. A. Sunlight assisted photocatalytic mineralization of nitrophenol isomers over W⁶⁺ impregnated ZnO. *Applied Catalysis B: Environmental*, 160-161, 227-239 (2014). <https://doi.org/10.1016/j.apcatb.2014.05.023>
- Harish, K. N., Naik, B., Kumar, P., Viswanath, R. Synthesis enhanced optical and photocatalytic study of Cd-Zn ferrites under sunlight. *Catalysis Science & Technology*, 2, 1022-1039 (2012). <https://doi.org/10.1039/c2cy00503d>
- Jang, J. S., Kim, H. G., Lee, J. S. Heterojunction semiconductors: A strategy to develop efficient photocatalytic materials for visible light water splitting. *Catalysis Today*, 185, 270-277 (2012). <https://doi.org/10.1016/j.cattod.2011.07.008>
- Kanade, K. G., Kale, B. B., Aiyer, R. C., Das, B. K. Effect of solvents on the synthesis of nano-size zinc oxide and its properties. *Materials Research Bulletin*, 41, 590-600 (2006). <https://doi.org/10.1016/j.materresbull.2005.09.002>
- Kayaci, F., Vempati, S., Donmez, I., Biyikliab, N., Uyar, T. Role of zinc interstitials and oxygen vacancies of ZnO in photocatalysis: a bottom-up approach to control defect density. *Nanoscale*, 6, 10224 (2014). <https://doi.org/10.1039/C4NR01887G>

- Kefeni, K. K., Mamba, B. B., Msagati, T. A. M. Application of spinel ferrite nanoparticles in water and wastewater treatment: A review. *Separation and Purification Technology*, 188, 399-422 (2017). <https://doi.org/10.1016/j.seppur.2017.07.015>
- Khan, A. A. K., Khalid, M. Synthesis of nano-sized ZnO and polyaniline-zinc oxide composite: characterization. stability in terms of DC electrical conductivity retention and application in ammonia vapor detection. *Journal of Applied Polymer Science*, 117, 1601-1607 (2010). <https://doi.org/10.1002/app.32037>
- Kumar, S. G., Rao, K. S. R. K. Zinc oxide based photocatalysis: tailoring surface bulk structure and related interfacial charge carrier dynamics for better environmental applications. *RSC Advances*, 5, 306-3351 (2015). <https://doi.org/10.1039/C4RA13299H>
- Lee, K. M., Lai, C. W., Ngai, K. S., Juan, J. C. Recent developments of zinc oxide based photocatalyst in water treatment technology: A review. *Water Research*, 88, 428-448 (2016). <https://doi.org/10.1016/j.watres.2015.09.045>
- Lee, W.H., Teh, S. J., Chou, P. M., Lai, C. W. Photocatalytic reduction of aqueous mercury (II) using hybrid WO₃-TiO₂ nonotubes film. *Current Nanoscience*, 13, 616-624 (2017). <https://doi.org/10.2174/1573413713666170616084447>
- Lenzi, G. G., Fávero, C. V. B., Colpini, L. M. S., Bernabe, H., Baesso, M. L., Specchia, S., Santos, O. A. A. Photocatalytic reduction of Hg (II) on TiO₂ and Ag/TiO₂ prepared by the sol-gel and impregnation methods. *Desalination*, 270, 241-247 (2011). <https://doi.org/10.1016/j.desal.2010.11.051>
- Li, J., Liu, Z., Zhu, Z. Magnetically separable ZnFe₂O₄, Fe₂O₃/ZnFe₂O₄ and ZnO/ZnFe₂O₄ hollow nanospheres with enhanced visible photocatalytic properties. *RSC Advances*, 4, 51302-51308 (2014). <https://doi.org/10.1039/C4RA06389A>
- Liu, D., Lv, Y., Zhang, M., Liu, Y., Zhu, Y., Zong, R., Zhu, Y. Defect-related photoluminescence and photocatalytic properties of porous ZnO nanosheets. *Journal of Materials Chemistry A*, 2, 15377-15388 (2014). <https://doi.org/10.1039/C4TA02678K>
- Liu, H., Hao, H., Xing, J., Dong, J., Zhang, Z., Zheng, Z., Zhao, K. Enhanced photocatalytic capability of zinc ferrite nanotube arrays decorated with gold nanoparticles for visible light-driven photodegradation of rhodamine B. *Journal of Material Science*, 51, 5872-5879 (2016). <https://doi.org/10.1007/s10853-016-9888-5>
- López-Muñoz, M. J., Aguado, J., Arencibia, A., Pascual, R. Mercury removal from aqueous solutions of HgCl₂ by heterogeneous photocatalysis with TiO₂. *Applied catalysis B: Environmental*, 104, 220-228 (2011). <https://doi.org/10.1016/j.apcatb.2011.03.029>
- Mandal, S., Natarajan, S. Adsorption and catalytic degradation of organic dyes in water using ZnO/Zn_xFe_{3-x}O₄ mixed oxides. *Journal of Environmental Chemical Engineering*, 3, 1185-1193 (2015). <https://doi.org/10.1016/j.jece.2015.04.021>
- Maya-Treviño, M. L., Villanueva-Rodríguez, M., Guzmán-Mar, J. L., Hinojosa-Reyes, L., Hernández-Ramírez, A. Comparison of the solar photocatalytic activity of ZnO-Fe₂O₃ and ZnO-Fe⁰ on 2,4-D degradation in a CPC reactor. *Photochemical & Photobiological Sciences*, 14, 543-549 (2015). <https://doi.org/10.1039/C4PP00274A>
- Mohamed, R. M., Gazzaz, H. A. Environmental remediation from aqueous mercury (II) by photocatalytic reduction using a coupled SnO₂-Co₃O₄ nanocomposite, *Desalination and Water Treatment*, 53, 2712-2719 (2015). <https://doi.org/10.1080/19443994.2013.871339>
- Mohamed, R. M., Salam, M. A. Photocatalytic reduction of aqueous mercury (II) using multi-walled carbon nanotubes Pd-ZnO nanocomposite. *Material Research Bulletin*, 50, 85-90 (2014). <https://doi.org/10.1016/j.materresbull.2013.10.031>
- Mudasir, M., Karelus, K., Aprilita, N. H., Wahyuni, E. T. Adsorption of mercury(II) on dithizone-immobilized natural zeolite. *Journal of Environmental Chemical Engineering*, 4, 1839-1849 (2016). <https://doi.org/10.1016/j.jece.2016.03.016>
- Music, S., Popovic, S., Maljkovic, M., Dragecivic, D. Influence of synthesis procedure on the formation and properties of zinc oxide. *Journal of Alloys and Compounds*, 347, 324-332 (2002). [https://doi.org/10.1016/S0925-8388\(02\)00792-2](https://doi.org/10.1016/S0925-8388(02)00792-2)
- Nirmala, M., Nair, M. G., Rekha, K., Anukaliani, A., Samdarshi, S. K., Nair, R. G. Photocatalytic activity of ZnO nanopowders Synthesized by DC Thermal Plasma. *African Journal of Basic & Applied Sciences*, 2, 161-166 (2010).
- Ong, C. B., Nb, L. Y., Mohammad, A. W. A review of ZnO nanoparticles as solar photocatalysts: Synthesis. mechanisms and applications. *Renewable and Sustainable Energy Reviews*, 81, 536-551 (2018). <https://doi.org/10.1016/j.rser.2017.08.020>
- Pandiyarajan, T., Udayabhaskar, R., Karthikeyan, B. Role of Fe doping on structural and vibrational properties of ZnO nanostructures. *Applied Physics A*, 107, 411-419 (2012). <https://doi.org/10.1007/s00339-011-6755-8>
- Pelaez, M., Nola, N. T., Pillai, S. C., Seery, M. K., Falaras, P., Kontos, A. G., Dunlop, P. S. M., Hamilton, J. W. J., Byrne, J. A., O'Shea, K., Enterazi, M. H., Dionysiou, D. D. A review on the visible light active titanium dioxide photocatalysts for environmental applications. *Applied Catalysis B: Environmental*, 125, 331-349 (2012). <https://doi.org/10.1016/j.apcatb.2012.05.036>

- Qamar, M. T., Aslam, M., Rehan, Z. A., Soomro, M. T., Basahi, J. M., Ismail, I. M. I., Hameed, A. The effect of Fe^{3+} based visible light receptive interfacial phases on the photocatalytic activity of ZnO for the removal of 2,4-dichlorophenoxy acetic acid in natural sunlight exposure. *Separation and Purification Technology*, 172, 512-528 (2017). <https://doi.org/10.1016/j.seppur.2016.08.030>
- Rahimi, R., Heidari-Golafzani, M., Rabbani, M. Preparation and photocatalytic application of $\text{Zn-Fe}_2\text{O}_4@ZnO$ core-shell nanostructures. *Superlattices and Microstructures*, 85, 497-503 (2015). <https://doi.org/10.1016/j.spmi.2015.05.047>
- Raja, K., Ramesh, P. S., Geetha, D. Structural, FTIR and photoluminescence studies of Fe doped ZnO nanopowder by co-precipitation method. *Spectrochimica Acta Part A: Molecular and Biomolecular Spectroscopy*, 131, 183-188 (2014). <https://doi.org/10.1016/j.saa.2014.03.047>
- Rahman, A. H. A., Teo, C. L., Idris, A., Misran, E., Asma, S., Leong, N. Polyvinyl alcohol-alginate ferrophoto gels for mercury (II) removal. *Journal of Industrial and Engineering Chemistry*, 33, 190-196 (2016). <https://doi.org/10.1016/j.jiec.2015.09.036>
- Rengaraj, S., Li, X. Z. Enhanced photocatalytic reduction reaction over Bi^{3+} - TiO_2 nanoparticles in presence of formic acid as a hole scavenger. *Chemosphere*, 66, 930-938 (2007). <https://doi.org/10.1016/j.chemosphere.2006.06.007>
- Sakthivel, S., Neppolian, B., Shankar, M. V., Arabindoo, B., Palanichamy, M., Murugesan, V. Solar photocatalytic degradation of azo dye: comparison of photocatalytic efficiency of ZnO and TiO_2 . *Solar Energy Materials & Solar Cells*, 77, 65-82 (2003). [https://doi.org/10.1016/S0927-0248\(02\)00255-6](https://doi.org/10.1016/S0927-0248(02)00255-6)
- Sheela, T., Nayaka, Y. A., Viswanatha, R., Basavanna, S., Venkatesha, T. G. Kinetics and thermodynamics studies on the adsorption of Zn(II), Cd(II) and Hg(II) from aqueous solution using zinc oxide nanoparticles. *Powder Technology*, 217, 163-170 (2012). <https://doi.org/10.1016/j.powtec.2011.10.023>
- Tadjarodi, A., Imani, M., Salehi, M. ZnFe_2O_4 nanoparticles and a clay encapsulated ZnFe_2O_4 nanocomposite: synthesis strategy, structural characteristics and the adsorption of dye pollutants in water. *RSC Advances*, 5, 56145-56156 (2015). <https://doi.org/10.1039/C5RA02163D>
- Xiao, M., Wang, Z., Lyu, M., Luo, B., Wang, S., Liu, G., Cheng, H., Wang, L. Hollow nanostructures for photocatalysis: advantages and challenges. *Advanced Materials*, 2018, 1801369-1801369 (2018). <https://doi.org/10.1002/adma.201801369>
- Wang, X., Pehkonen, S. O., Ray, A. K. Photocatalytic reduction of Hg(II) on two commercial TiO_2 catalysts. *Electrochimica Acta*, 49, 1435-1444 (2004). [https://doi.org/10.1016/S0013-4686\(03\)00907-1](https://doi.org/10.1016/S0013-4686(03)00907-1)
- Wang, Y., Wang, Q., Zhan, X., Wang, F., Safdar, M., He, J. Visible light driven type II heterostructures and their enhanced photocatalysis properties: a review. *Nanoscale*, 5, 8326-8339 (2013). <https://doi.org/10.1039/c3nr01577g>
- Zhou, C., Zhu, H., Wang, Q., Wang, J., Cheng, J., Guo, Y., Zhou, X., Bai, R. Adsorption of mercury (II) with an Fe_3O_4 magnetic polypyrrole-graphene oxide nanocomposite. *RSC Advances*, 7, 18466-18479 (2017). <https://doi.org/10.1039/C7RA01147D>
- Zhu, K., Wang, J., Wang, Y., Jin, C., Ganeshraja, A. S. Visible-light-induced photocatalysis and peroxy monosulfate activation over ZnFe_2O_4 fine nanoparticles for degradation of Orange. *Catalysis Science & Technology*, 6, 2296 (2016). <https://doi.org/10.1039/C5CY01735A>